# Stacking Structures of Few-Layer Graphene Revealed by Phase-Sensitive Infrared Nanoscopy

Deok-Soo Kim,[†,○] Hyuksang Kwon,[†,¶,○] Alexey Yu. Nikitin,[‡,§] Seongjin Ahn,[∥] Luis Martín-Moreno,[⊥] Francisco J. García-Vidal,[#] Sunmin Ryu,[▽] Hongki Min,[∥] and Zee Hwan Kim*[,†]

[†]Department of Chemistry, Seoul National University, Seoul 136-701, Korea, [‡]CIC nanoGUNE Consolider, 20018 Donostia-San Sebastian, Spain, [§]IKERBASQUE Basque Foundation for Science, 48011 Bilbao, Spain, [∥]Department of Physics and Astronomy, Seoul National University, Seoul 446-701, Korea, [⊥]Instituto de Ciencia de Materiales de Aragón and Departamento de Física de la Materia Condensada, CSIC—Universidad de Zaragoza, E-50009 Zaragoza, Spain, [#]Departamento de Física Teórica de la Materia Condensada and Condensed Matter Physics Center (IFIMAC), Universidad Autónoma de Madrid, E-28049 Madrid, Spain, and [▽]Department of Chemistry, Pohang University of Science and Technology (POSTECH), Pohang, Gyeongbuk 790-784, Korea. [○]These authors contributed equally. [¶]Present address: Center for Nano-Bio Measurement, Korea Research Institute of Standards and Science, Daejeon 305-340, Korea.

**ABSTRACT** The stacking orders in few-layer graphene (FLG) strongly influences the electronic properties of the material. To explore the stacking-specific properties of FLG in detail, one needs powerful microscopy techniques that visualize stacking domains with sufficient spatial resolution. We demonstrate that infrared (IR) scattering scanning near-field optical microscopy (sSNOM) directly



maps out the stacking domains of FLG with a nanometric resolution, based on the stacking-specific IR conductivities of FLG. The intensity and phase contrasts of sSNOM are compared with the sSNOM contrast model, which is based on the dipolar tip—sample coupling and the theoretical conductivity spectra of FLG, allowing a clear assignment of each FLG domain as Bernal, rhombohedral, or intermediate stacks for tri-, tetra-, and pentalayer graphene. The method offers 10—100 times better spatial resolution than the far-field Raman and infrared spectroscopic methods, yet it allows far more experimental flexibility than the scanning tunneling microscopy and electron microscopy.
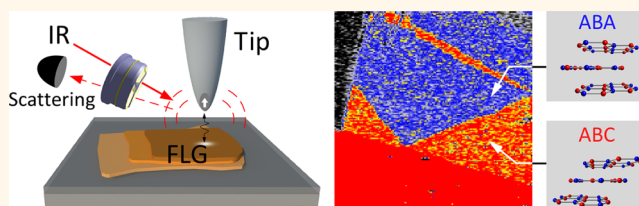
**KEYWORDS:** nanoplasmonics · near-field optics · nanoscopy · multilayer graphene · stacking orders

S̲ubtle changes of stacking orders in few-layer graphene (FLG) bring drastic changes in band structures,[1−6] electrical[7] and magnetic properties.[8,9] In particular, trilayer graphene (TLG, upper panel of Figure 1a) can assume the ABA (Bernal) structure, which is semimetallic, and the ABC (rhombohedral) structure, which is semiconducting.[2,10] More diverse structure-specific properties, which are currently largely unexplored, are expected for FLG with more than three layers. Besides pure academic interest, such stacking-specific properties of FLG also hold a great promise for developing new electronic and optoelectronic devices because FLG with specific stacking orders allows a large band gap that can be manipulated by an external electric field.[3,11,12] The FLG samples are usually made of domains of various stacking orders. Therefore, a full realization of such promise requires detailed knowledge on the formation

and interconversion[13,14] of stacking orders, structures of the stacking domain boundaries[13,14] and their influence on transport properties, which calls for powerful microscopy techniques that can directly visualize and identify the domains.

High-resolution electron microscopy[15−18] and scanning tunneling microscopy[14] successfully visualizes stacking domains and their boundaries with ∼1 nm resolution, but they are restricted to the samples on conducting substrate, or to the ones in free-standing conditions. The line shape analyses of Raman spectra[19,20] provide a convenient means to differentiate Bernal/rhombohedral domains of FLG with ∼1 μm resolution. While this technique is generally applicable to FLG on any substrates, the analysis becomes progressively more challenging as we increase the number of layers. The far-field infrared (IR) spectroscopy delivers direct information[3,5] on stacking orders through
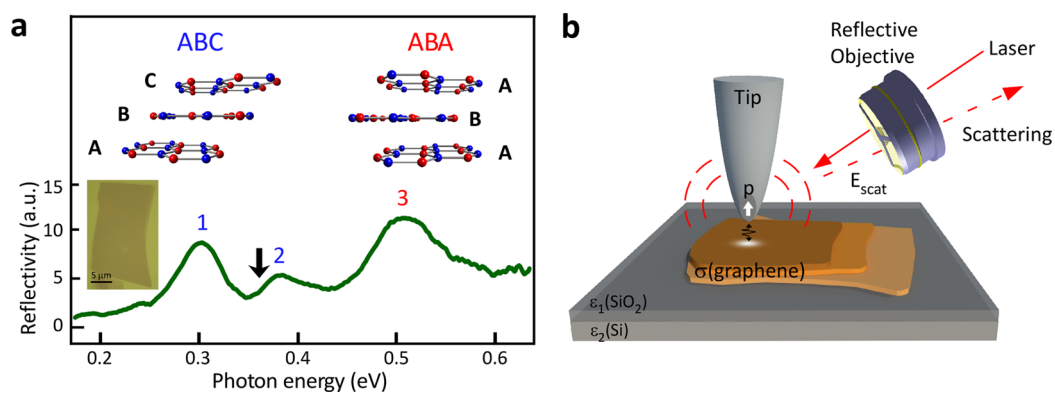
**Figure 1. Spectrum of trilayer graphene and schematic of sSNOM measurement.** (a) Rhombohedral (ABC) and Bernal (ABA) stacking structures of a trilayer graphene (TLG, top panel) and an IR reflection spectrum (bottom panel) obtained from a mechanically exfoliated TLG on a SiO$_2$/Si substrate shown in the inset optical reflection image. The spatial resolution of the micro-IR spectrometer employed is $\sim$10 $\mu$m, which is insufficient to resolve stacking domains in TLG. Thus, the spectrum represents the weighted average of the spectra of ABA and ABC domains in the TLG. Peaks 1 and 2 arise from the ABC-structure, whereas peak 3 originates from the ABA structure. The black arrow points to the photon energy ($\varepsilon_{phot}$ = 0.366 eV) employed for the IR-sSNOM measurement, which is resonant with an IR transition of the ABC-structure. (b) Schematic of sSNOM measurements of the FLG sample.

the stacking-dependent IR-conductivity spectra ($\sigma$).[4,5] Unfortunately, the spatial resolution (5−10 $\mu$m) of far-field IR spectro-microscopy is insufficient to spatially resolve the stacking domains.

Here, we report that the IR scattering scanning near-field optical microscopy (sSNOM)[21−30] enables a direct, nanometric visualization and characterization of the stacking domains in FLG. The comparison of the experimental contrast (intensity and phase) and the sSNOM contrast, which is based on the dipolar tip−sample coupling and theoretical complex conductivity spectra of FLG, allow us to uniquely assign stacking orders of domains in tri-, tetra-, and pentalayer FLG as Bernal, rhombohedral, or intermediate structures. The model also reveals that it is the two-dimensional nature of FLG leading to the remarkably large contrast difference for differently stacked FLG. These attributes complement the limits of existing methods for studying the stacking orders of FLG.

## RESULTS AND DISCUSSION

Figure 1a (bottom panel) shows an IR reflection spectrum of a mechanically exfoliated TLG on a SiO$_2$/Si substrate (shown in the inset photograph) displaying characteristic resonances in optical conductivities arising from the interband transitions of the ABC (0.3 and 0.38 eV) and ABA (0.5 eV) domains.[3,4,20] For sSNOM measurements below, we use the IR-light at 0.366 eV, which is resonant with a transition of ABC-TLG (marked as an arrow in Figure 1a). The sSNOM measures (see schematic in Figure 1b and Methods section) the scattering ($E_{scat}$) from a laser-illuminated junction made of a metallic tip (in our case, an atomic force micro-scope, AFM, probe) and the sample surface. The local optical property of the surface influences the tip−sample coupling, and thus determines the $E_{scat}$ and sSNOM contrast. For a FLG sample, differently stacked

layers exhibit different in-plane IR conductivities ($\sigma$),[3−5] therefore, providing stacking-specific sSNOM contrasts. Experimentally, the lock-in filtered (at the third harmonic frequency of the tip's oscillation) scattering amplitude $s_3 = |s_3|e^{i\phi_3}$ of $E_{scat}$ is used instead to avoid the far-field background.

Figure 2 compares the AFM (Topo), the optical reflection (OR) and sSNOM ($|s_3|^2$ and $\phi_3$) images of a mechanically exfoliated FLG on a SiO$_2$/Si substrate. To facilitate the experiment-model comparison of sSNOM amplitudes, we will present the experimental and model sSNOM signals that are normalized with respect to those of bare SiO$_2$/Si substrate: $|s_3|^2 = |s_3$ (FLG on substrate)/ $s_3$ (substrate)$|^2$ and $\phi_3 = \phi_3$ (FLG on substrate) $- \phi_3$ (substrate). The topography (Figure 2a) and optical reflection (Figure 2b) images show homogeneous profiles throughout the entire region of the TLG. On the other hand, the intensity and phase sSNOM images (Figure 2c,e) obtained with a resonant IR-light show two distinct domains. Similar features are consistently found in the sSNOM images of other TLG samples examined (see Supporting Information-A). The features are com-pletely absent in the sSNOM image of the same TLG obtained with light at $\lambda$ = 633 nm (1.96 eV, Figure 2d). We interpret that the features in IR-sSNOM images are the ABA (darker intensity) and ABC (brighter intensity) stacking domains of TLG, which will be validated by the tip−sample near-field coupling model described below. The interpretation is also corroborated by a subtle change in line-shape of the 2D peaks of Raman spectra[20] measured on the two regions of the same TLG (see Supporting Information-B). The ABA/ABC boundaries in the IR-sSNOM images have a transitional half-width of $\sim$40 nm (see Figure 2f,g). The finite domain wall thickness[14] of the ABA/ABC boundaries as well as the native sSNOM resolution (typically 10−50 nm) may contribute to the observed width of the transition.
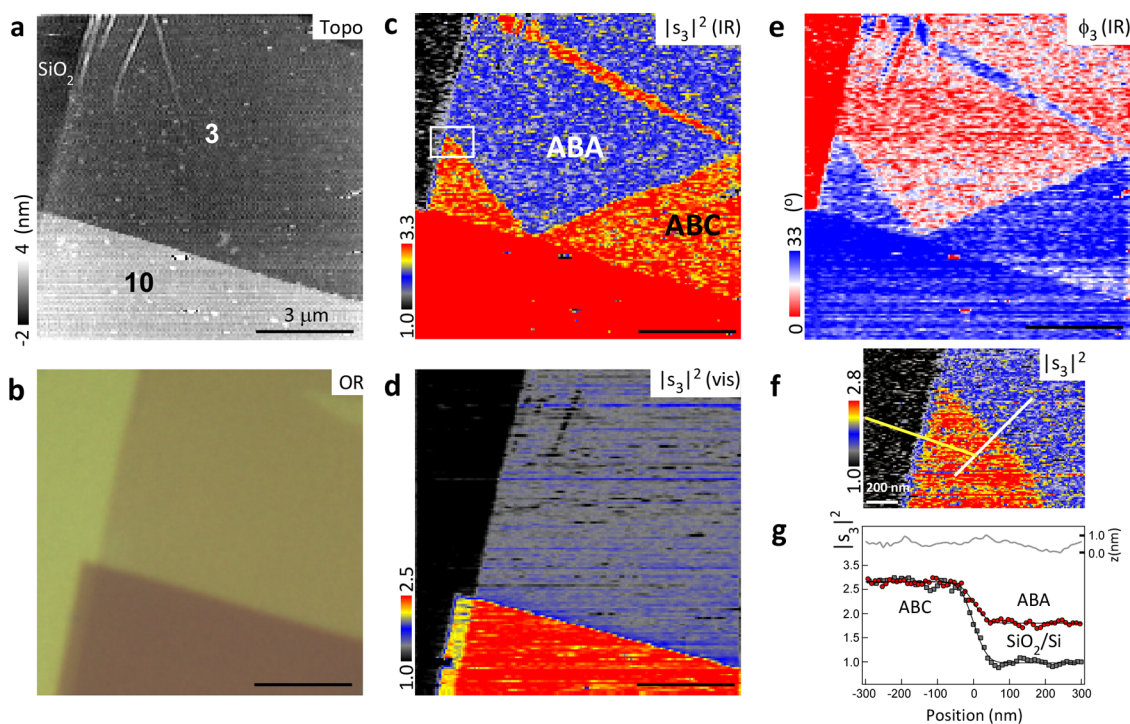
**Figure 2. Stacking-specific sSNOM images of a trilayer graphene.** (a) Topography. The numbers ($n$) refer to the number of graphene layers ($n = 3$ and $10$). The number of layers, $n$, is determined by a separate Raman spectroscopy measurement (using the G and 2D peaks) and by AFM topography (0.34 nm per layer). (b) Far-field optical reflection image (OR) obtained with a white-light source. (c) sSNOM intensity ($|s_3|^2$) obtained with $\lambda = 3.39\ \mu$m light (0.366 eV). (d) sSNOM intensity image obtained with a visible light ($\lambda = 633$ nm, 1.96 eV). (e) sSNOM phase image at $\lambda = 3.39\ \mu$m. (f) Zoom-in scan of the region marked with a rectangle in (c). (g) Line-profiles of sSNOM intensity (red circles) and the corresponding topography (gray curve) across the ABA−ABC domain boundary indicated in (f) with a white line. Also shown as a comparison is the line-profile sampled across the ABC/bare substrate (SiO$_2$/Si) boundary (gray squares) indicated in (f) with a yellow line. The black solid curves are the fit of the signals to an error-function.

For the particular sSNOM images shown, however, we believe that the width mostly reflects the resolution of sSNOM because we observe nearly the same transitional width across the ABC/bare substrate (SiO$_2$/Si) boundary (see Figure 2g and Supporting Information-C for more detail).

To fully validate the domain assignment in TLG and thicker FLG, we have modeled the sSNOM signals of FLG based on tip−sample dipolar coupling[26] (see Methods and Supporting Information-D), which includes the following: the incident light induces an oscillating point-dipole at the tip (with a dipole moment $\mathbf{p}_0$), the tip-dipole polarizes the sample surface, and the polarized charges of the surface alter the tip-dipole creating a new tip-dipole $\mathbf{p}$. The $E_{\text{scat}}$ from the tip-dipole and thus the $s_3$ are altered by the local properties of the sample surface (see Figure 1b).

Experimentally, we find that the normalized sSNOM contrasts show significant tip-to-tip variation (up to 40% in intensity), which primarily arise from the variations in the radius of curvature of tip-end and the tip−sample feedback condition. Nevertheless, the relative contrasts and their ordering remain stable within the time scale of measurement. To account for such experimental variation, the average tip−sample distance ($z$) and the radius of the tip-end ($a$) are set as

adjustable (within a physically relevant range) fitting parameters. In the sSNOM contrast model, the tip-end is modeled as a nanosphere, whereas the real tip-end is better characterized as a cone. Therefore, the model $a$ and $z$ do not necessarily correspond to the real topographic shape of the tip-end and tip−sample distance, respectively (see Supporting Information-D for more detail). This requires the adjustment of the model tip-parameters. More often than not, the tip picks up impurity particles (such as polymer debris or inorganic dirt), which drastically alters the sSNOM contrasts. The images obtained with such contaminated tip-end, which can be readily recognized by the topographic changes, are discarded.

The complete experimental complex conductivities of FLG with various stacking orders, which are the essential input parameters of the simulation, are currently experimentally unavailable. The only available experimental conductivities are the real part of the conductivities of Bernal-stacked FLG ($n = 1-6$) and rhombohedral TLG obtained by Heinz and co-workers.[3−5,20,31] Thus, we theoretically calculated the complex conductivities of FLG based on the tight-binding Hamiltonian[6] and the Kubo formula[32] (see Supporting Information-E), which is displayed in Figure 3. The matrix elements ($\gamma_0$ and $\gamma_1$) and the parameters for the Kubo formula
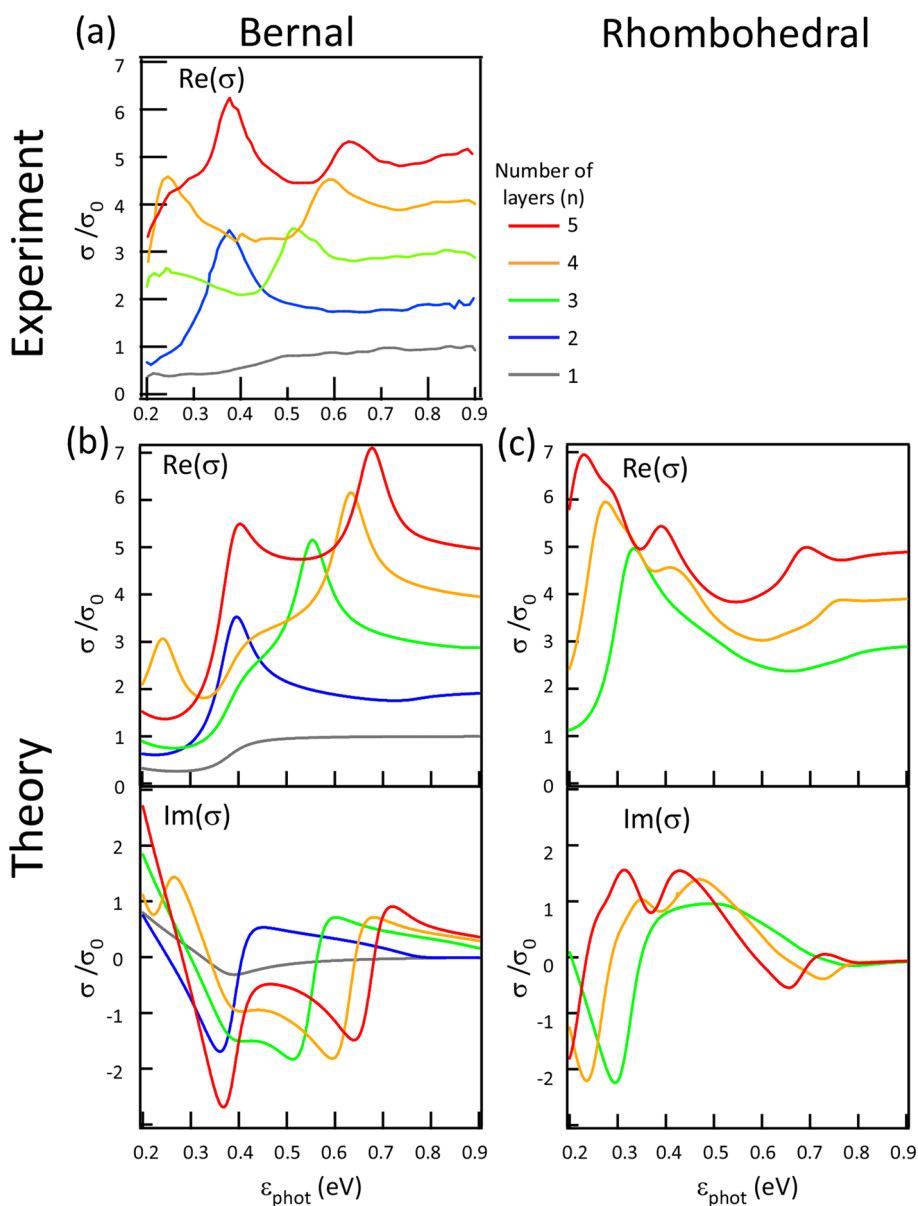
**Figure 3. Complex optical conductivity spectra of FLG. (a) Experimental conductivity (real) spectra of Bernal-stacked FLG obtained by Heinz and co-workers.[4] (b) Real (upper panel) and imaginary (lower panel) parts of the conductivity spectra of Bernal-stacked FLG calculated from tight-binding Hamiltonian and Kubo formula. (c) Theoretical conductivity spectra of rhombohedral FLG. All of the conductivities ($\sigma$) are expressed in unit of $\sigma_0 = c\alpha/4$, where $c$ and $\alpha$ are the speed of light and the fine-structure constant.**

(phenomenological disorder parameter $\eta = 40$ meV, and Fermi energy $E_f = 0.19$ eV, which is estimated by analyzing the Raman spectra; see Supporting Information-F) are chosen so the theoretical (Figure 3b) and experimental spectra[4] of Bernal-stacked FLG (Figure 3a) show closest match. The same set of parameters is used for calculating the conductivities of all of the rhombohedral (Figure 3c) and intermediate-stack (not shown) FLG considered. These theoretical complex conductivity spectra of FLG, together with the dielectric functions of the substrate materials ($SiO_2$ and Si), are used to evaluate the sSNOM model contrasts.

Figure 4b shows the sSNOM model signals of ABA- and ABC- TLG plotted as a function of photon energy

($\varepsilon_{phot}$), along with the experimental signals of the two domains at $\varepsilon_{phot} = 0.366$ and 1.96 eV. The theoretical conductivity spectra of TLG are also drawn in Figure 4a for comparison. With $\varepsilon_{phot} = 0.366$ eV, the conductivities of the ABA- and ABC-TLG are significantly different, leading to large sSNOM contrast difference between the two. With $\varepsilon_{phot} = 1.96$ eV, however, the conductivities of the two are essentially the same and the contrast difference vanishes (Figure 2d).

In modeling the sSNOM contrast, the tip-parameters (effective radius of curvature of the tip-end and the average tip−sample distance) of the model are adjusted (to within physically relevant ranges) to give the best match with the observed intensity ($|s_3|^2$) contrasts
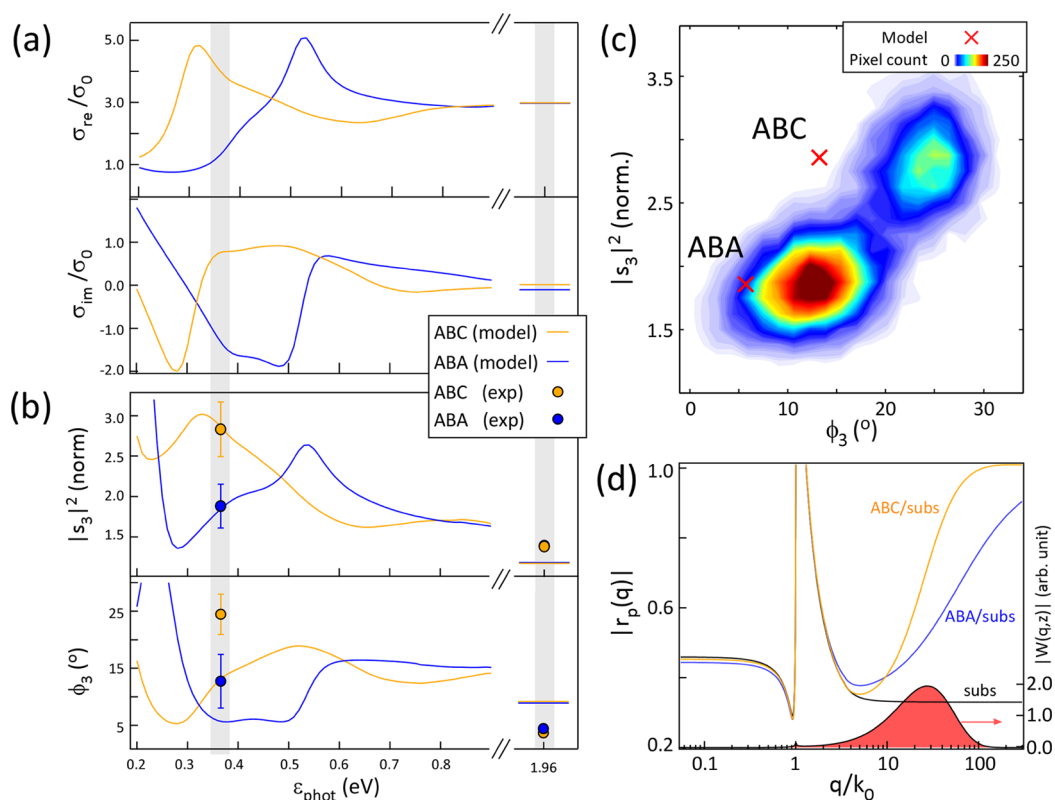
**Figure 4. Comparison of the experimental and model sSNOM contrasts.** (a) Theoretical spectra of the real (upper panel) and the imaginary (lower panel) parts of the optical conductivity of TLG. The conductivities are expressed in unit of $\sigma_0 = c\alpha/4$, where $c$ and $\alpha$ are the speed of light and the fine-structure constant, respectively. (b) Modeled sSNOM intensity (upper panel) and phase (lower panel) of ABA- and ABC-TLG plotted as a function of photon energy ($\varepsilon_{phot}$). The experimental sSNOM contrasts at $\varepsilon_{phot} = 0.366$ and 1.96 eV are also plotted using filled circles. The error bars of the experimental signals correspond to twice the standard deviation of the signals within the ABA or ABC-domains. (c) The two-dimensional sSNOM image histogram ($\phi_3$, $|s_3|^2$) extracted from the TLG regions of Figure 2c,e. The modeled contrasts of the ABA and ABC structures evaluated at $\varepsilon_{phot} = 0.366$ eV are displayed as crosses. In both b and c, the signals of the TLGs are normalized with respect to those of the substrate ($SiO_2/Si$). (d) Norms of the p-polarized Fresnel coefficient $r_p(q)$ for ABA/$SiO_2$/Si (blue), ABC/$SiO_2$/Si (yellow), and $SiO_2$/Si (black) are plotted as a function of the in-plane photon momentum $q/k_0$, where $k_0 = \omega/c$ ($\omega$ and $c$ are the angular frequency and speed of light, respectively). Also shown as a filled curve (red) is the norm of weight function $W(q, z)$ (see main text) at $\varepsilon_{phot} = 0.366$ eV with a tip–sample distance $z = 20$ nm, which determines the range of $q$'s that are sampled by sSNOM tip.

for ABA and ABC domains. The resulting sSNOM model contrasts offer agreement with experiment that is quantitative for $|s_3|^2$, qualitative for $\phi_3$, and semiquantitative for the phase difference $\phi_{3,ABC} - \phi_{3,ABA}$ (+11.7° and +7.3° for experiment and model, respectively). By adjusting the Hamiltonian matrix elements ($\gamma_0$ and $\gamma_1$) as well as the tip-parameters, we could obtain better agreement in phase contrasts of TLG. However, such optimized Hamiltonian matrix elements give overall inferior fit to the sSNOM intensity and phases contrasts of all FLG ($n = 1-5$), and thus they are not used in the modeling of sSNOM contrasts of TLG and thicker FLG.

We believe that the limited accuracies of model conductivities (including the neglect of electrostatic perturbation from the substrate on the TLG band structure[3]) and point-dipole approximation of the tip, together with the possible systematic measurement error, may contribute to the discrepancies. As shown in Figure S7 of Supporting Information-D, the visible contrasts of FLG also show similar systematic disagreement

in sSNOM phase, indicating that the deviation may originate either from the tip–sample coupling model or from the measurement error, because the conductivities of FLG at visible frequencies are only dependent on the number of layers. At the same time, we find that the sSNOM phases of FLG are more sensitive to the variation in conductivities than in the case of sSNOM intensities. For example, as shown in Supporting Information-G, sSNOM model contrasts of FLG show drastic variation in sSNOM phase with respect to the Fermi level change (i.e., doping level change), indicating that the observed disagreement may reflect the inaccuracies of modeled conductivities of FLG.

While a more sophisticated modeling of the sSNOM tip[33,34] and the TLG band-structure should improve the agreement, the current model is already sufficient for assigning the stacking orders of TLG, especially with the help of combined intensity and phase sSNOM contrast information.[35] Figure 4c shows a two-dimensional ($\phi_3$, $|s_3|^2$) image histogram of sSNOM
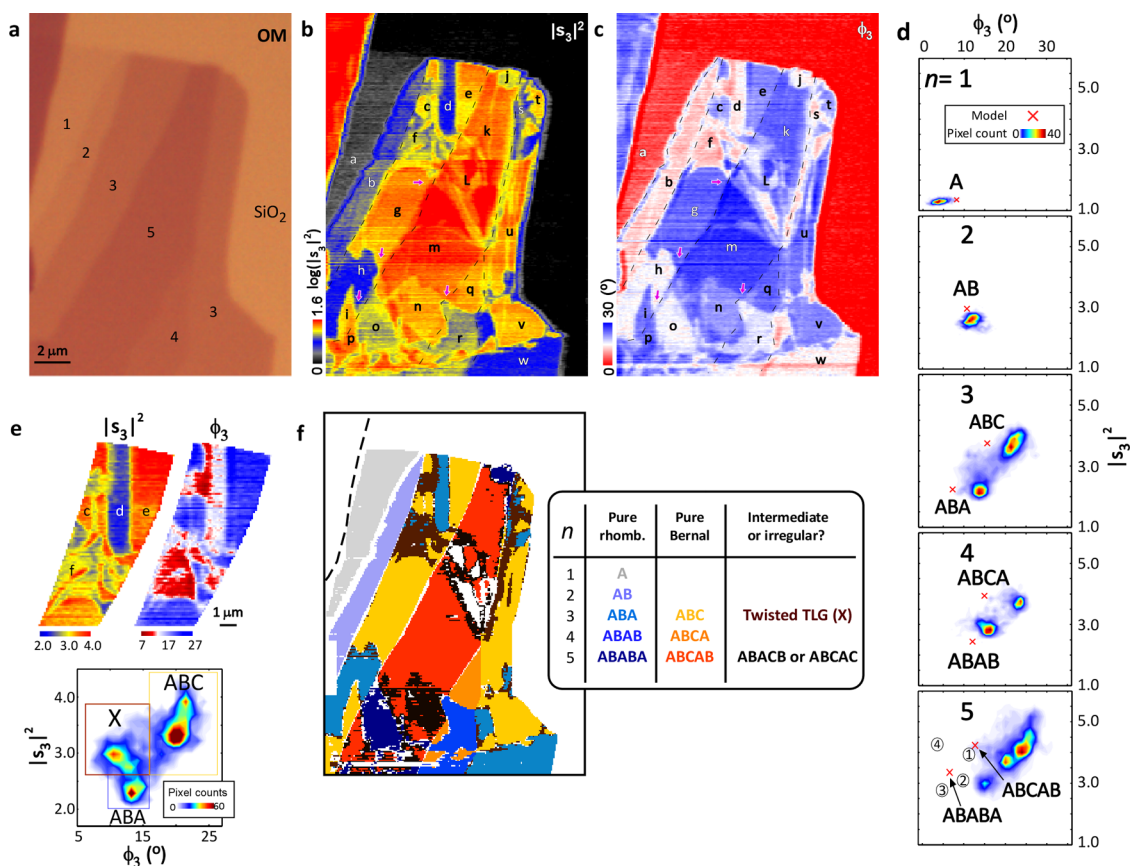
**Figure 5.** IR-sSNOM of $n = 1-5$ layers. (a) Optical reflection microscopy (OM) image. (b) sSNOM intensity ($|s_3|^2$) obtained at $\varepsilon_{phot} = 0.366$ eV. (c) sSNOM phase. (d) 2D ($\phi_3$, $|s_3|^2$) image histogram sampled from (b) and (c) displayed with the sSNOM model prediction (red crosses) based on pure Bernal and pure rhombohedral structures. In the histogram for 5-layer, the modeled sSNOM contrasts for various intermediate stacks are also shown as circled numbers: ABACB and ABCAC (1), ABABC and ABCBC (2), ABACA (3), and ABCBA (4). (e) sSNOM intensity and phase images of the trilayer cropped from Figure 4b and c (around c, d, e and f regions) with reduced color ranges (see the color bars) and 2D image histograms of the corresponding region of the sample. (f) Final assignment of the stacking structures of (b) and (c). The color-code of the domains (figure) corresponds to the structural assignments written in the same color in the inset table.

signals sampled from the TLG in Figure 2c,e, along with the model predictions at $\varepsilon_{phot} = 0.366$ eV, which allows a clear visual identification of the two regions as ABA and ABC domains, despite the significant disagreement in phase contrasts.

We also recognize that it is the two-dimensional optical response of graphene producing large sensitivity and selectivity of the sSNOM signals of the FLG. The sSNOM amplitude is governed by the evanescent component of the p-polarized Fresnel coefficient $r_p(q)$ (where $q$ is the in-plane photon momentum) of the sample surface. With the tip located at $z = 20$ nm above the sample surface, the tip preferentially probes $r_p(q)$ with $q/k_0 = 10-100$ (where $k_0$ is the magnitude of the wave vector of the IR-light), as determined by the magnitude of a complex weighting function,[23,36] $W(q, z) = r_p(q)q^3 e^{2iz(k_0^2-q^2)^{1/2}}/(k_0^2 - q^2)^{1/2}$ (see Figure 4d and Supporting Information-D). Because of the dominant in-plane optical conductivity of graphene, the $r_p(q)$ of the FLG/substrate rapidly increases toward unity (i. e., it becomes a perfect reflector) with the increase in $q$ (see Figure 4d for $r_p(q)$ of ABA- and ABC-TLG on an SiO$_2$/Si

substrate). This causes the enhanced sensitivity and the structural selectivity of the sSNOM signal, which is not possible for far-field imaging ($q \sim 0$) or sSNOM imaging of three-dimensional (or isotropic) nano-objects.

Note that the imaging modality of sSNOM of FLG is entirely different to that of the reports by Basov and co-workers,[22,23,27] Hillenbrand and co-workers,[21,28] and Raschke and co-workers,[35] who used the same sSNOM technique to visualize the surface plasmon polaritons (SPPs) on graphene. Under their measurement condition ($\varepsilon_{phot} \sim 0.1$ eV), the graphene supports the propagating SPP and the tip launches and detects the SPP. With $\varepsilon_{phot} \sim 0.366$ eV (current photon energy), however, the SPPs do not propagate on the FLG, and the sSNOM visualizes only the local conductivities.

A very unique aspect of our study is that the sSNOM stacking mapping can also be successfully applied to FLG with any number of layers, provided that differently stacked domains show distinct conductivities. To demonstrate such capability, we have shown a set of IR-sSNOM images of FLG with 1−5 layers, revealing complex features (Figure 5b,c) hidden behind a seemingly

uniform topographic shapes (as seen by the optical reflection image in Figure 5a). The image histograms (Figure 5d) show a single peak for mono- and bilayers, double peaks for tri- and tetra-layers, and triple peaks for pentalayers. With the exception of the pentalayers, the numbers of peaks (*i.e.*, number of distinct domains) are consistent with a general belief that mechanically exfoliated FLG exists either as a pure Bernal or a pure rhombohedral structure. Moreover, the peak positions in the histograms closely match the sSNOM model predictions of pure Bernal and pure rhombohedral structures (shown in red-crosses in the histograms), confirming that most of the features arise from Bernal or rhombohedral stacks.

Interestingly, the sSNOM also identifies nonregular domains besides pure Bernal or pure rhombohedral domains. Here, we show two such examples. The pentalayer in Figure 5 shows at least three domains, which can be recognized by the triple peaks in the histogram and by the three different contrasts in the m-, n-, and o-regions in Figure 5b,c. We note that the boundaries m/n and n/o (marked with arrows in Figure 5b,c) smoothly translate to the neighboring q/r (assigned as ABCA/ABAB) and g/h (assigned as ABC/ABA) boundaries. Thus, we conclude that they are three different stacking domains, where at least one of them is an intermediate stacking domain (for example ABABC). As displayed in the image histogram of the pentalayer (bottom panel of Figure 5d), the phase disagreement between the experiment and the model (5−10°) is comparable to the modeled contrast differences among the eight possible stacking orders of the pentalayer, making it hard to assign the stacking sequences of the three domains. Here, we use the $|s_3|^2$ to tentatively determine that the m- and o-domains are ABCAB and ABABA stacks, respectively, and that the n-domain is an intermediate stacking domain, possibly an ABACB or an ABCAC stack. In Figure 5e, we redrew the c-, d-, e-, and f-regions of the TLG of Figure 5b,c with a reduced color-range. The image and the associated histogram (bottom panel of Figure 5e) show the presence of an extra domain (denoted as X) distinct from the ABA or ABC domains. Currently, we do not have sufficient information to reveal the nature of the domain. One possibility is the twisted TLG,[16] in which one of the layers has a mismatched orientation with respect to the other two layers. By comparing the 2D intensity-phase histogram and the sSNOM model contrasts, we were able to assign >80% of the FLG domains observed as pure Bernal, pure rhombohedral, or intermediate stacking structures. The overall assignment of the domain is shown in Figure 5f as a color-code domain map and a table.

## CONCLUSIONS

To sum up, we have demonstrated that sSNOM with a resonant IR-light can visualize and characterize stacking domains of FLG with a ∼40 nm spatial resolution. While the data shown above is mainly for the graphene sample exfoliated from bulk graphites, the same measurement could be also carried out for the graphene samples generated by chemical vapor deposition (CVD) method. In fact, we have already obtained preliminary sSNOM images (not shown) of CVD graphene, which clearly show stacking domains. The sSNOM stacking map offers ∼10 and ∼100 times better spatial resolution than the one available from Raman and IR spectroscopic methods, respectively. Because it is an optical technique, the sSNOM can be applied to FLG on dielectric substrates, as well as metallic substrates. Therefore, this technique offers a major practical advantage over scanning tunneling microscopy and electron microscopy. This is particularly relevant for *in situ* characterization of the FLG-devices, most of which is done on dielectric substrates.

In its essence, the IR-sSNOM contrast of FLG shown above arises from the local conductivity difference. Thus, in principle, it can also visualize and characterize any local properties (such as strain, doping, and chemical functionalization) inducing changes in local conductivities. Current work relies on the sSNOM contrasts at fixed IR (resonant at rhombohedral structure) and visible (reference) wavelengths, severely keeping us from identifying more complex local structures. We believe that sSNOM measurements with two IR lasers near 0.36 eV (resonating with rhombohedral structures) and 0.6 eV (resonating with Bernal structures) may provide two sets of complementary sSNOM images of the pure rhombohedral and Bernal components, removing significant portion of uncertainties in the structural assignment of FLG domains. Ultimately, a full spectroscopic sSNOM with a tunable laser,[23,24] which is a straightforward extension of the current study, will provide more complete information on local structures of FLG.

As mentioned above, the complex optical conductivities of variously stacked FLG are largely unknown, and thus, we had to rely on the theoretically derived conductivities to model the sSNOM contrasts. The main reason for the missing conductivity spectra for FLG is that the sizes of specific stacking domains can be significantly smaller than the diffraction limited far-field IR beam of conventional IR spectroscopy, preventing the reliable extraction of stacking-dependent conductivities. For example, with a far-field IR spectroscopy, it is not straightforward to obtain the conductivities of intermediate stack FLG domains because they are not abundant in mechanically exfoliated, or chemically grown graphene. As shown above, on the other hand, the sSNOM can identify small, less abundant stacking domains in FLG. Therefore, we believe that the sSNOM can be an excellent alternative method measuring the conductivities of less abundant stacking structures.

Finally, we note that the method does not rely on any special properties of FLG besides the stacking-specific in-plane conductivities. In this regard, the results also demonstrate that the sSNOM offers the excellent sensitivity, spectral selectivity, and nanometric resolution that are needed for nanospectroscopic exploration of two-dimensional nanomaterials in general.

## METHODS

**Sample.** The FLG samples are prepared by mechanically exfoliating kish-graphite and transferring to a $SiO_2$ (thickness of 285 nm)/Si substrate. Micro-Raman spectroscopy measurements (an excitation wavelength of 514.5 nm) are carried out on the sample to determine the number of layers ($n$) and to provide low-resolution assignments of ABA or ABC domains in TLG.

**Measurement.** We use the side-illuminated sSNOM[25] setup (see Figure 1b of main text), which consists of a tapping-mode atomic force microscope (AFM), cw-lasers (HeNe, $\lambda = 633$ nm and $\lambda = 3.39$ $\mu$m), a Michelson interferometer, and an InSb detector cooled with liquid-nitrogen. For the particular experiment, we used the home-built sSNOM setup, but equally good or even better sSNOM images of FLG may be obtained with a commercial sSNOM setup[37] as well. A PtIr coated AFM tip (Nanosensors, PPP-NCHPt) is dithered near the resonance frequency of an AFM-cantilever ($\Omega \sim 300$ kHz) with a full amplitude of $20-100$ nm above the sample surface. Linearly polarized (p-polarized with respect to the sample surface) light from the laser is focused on the tip—sample junction with an angle of 30° with respect to the sample surface *via* a reflective objective (Schwarzschild objective). Scattered light from the tip—sample junction is collected by the same objective. The collected light is interferometrically amplified and detected by the InSb detector, and the detected signal is lock-in filtered at the third harmonic ($3\Omega \sim 900$ kHz) of the tip oscillation to give the intensity ($|s_3|^2$) and phase ($\phi_3$) of the demodulated complex amplitude ($s_3 = |s_3|e^{i\phi_3}$). For the interferometric amplification, we employed the two-phase homodyne method, in which two sSNOM line-scans of the same regions of the sample are recorded with the interferometer mirror positioned at 0 and $\lambda/8$ positions, and the two are processed to construct the intensity and phase sSNOM data.

**Model.** Two key assumptions are made in modeling the sSNOM signal of the FLG: the tip-end is approximated to a nanosphere with a radius $a$ that can generate a point-dipole upon light illumination, and the thickness of the FLG is assumed to be zero. The radius of the tip-end does not necessarily represent the actual curvature of the tip-end; thus, we treat the tip-parameters to be adjustable (within the physically relevant range) parameters of model. The scattering ($E_{scat}$ and $s_3$) from the tip—sample coupling is obtained by numerically evaluating the Green's dyadic function.[26] The $SiO_2$ (thickness of 285 nm)/Si interface is explicitly taken into account in the model, although the $E_{scat}$ and the $s_3$ are fairly similar to the ones without the interface.[26,38] See Supporting Information-D for more detail.

*Conflict of Interest:* The authors declare no competing financial interest.

*Supporting Information Available:* Details of theoretical optical conductivities of FLG, point-dipole scattering model of sSNOM, additional IR and visible sSNOM images of FLG, and the estimation of substrate-induced spontaneous doping of graphenes are provided. The Supporting Information is available free of charge on the ACS Publications website at DOI: 10.1021/acsnano.5b02813.

## REFERENCES AND NOTES

1. Bao, W.; Jing, L.; Velasco, J., Jr.; Lee, Y.; Liu, G.; Tran, D.; Standley, B.; Aykol, M.; Cronin, S. B.; Smirnov, D.; et al. Stacking-Dependent Band Gap and Quantum Transport in Trilayer Graphene. *Nat. Phys.* **2011**, *7*, 948–952.
2. Latil, S.; Henrard, L. Charge Carriers in Few-Layer Graphene Films. *Phys. Rev. Lett.* **2006**, *97*, 036803.
3. Lui, C. H.; Li, Z.; Mak, K. F.; Cappelluti, E.; Heinz, T. F. Observation of an Electrically Tunable Band Gap in Trilayer Graphene. *Nat. Phys.* **2011**, *7*, 944–947.
4. Mak, K. F.; Sfeir, M. Y.; Misewich, J. A.; Heinz, T. F. The Evolution of Electronic Structure in Few-Layer Graphene Revealed by Optical Spectroscopy. *Proc. Natl. Acad. Sci. U.S.A.* **2010**, *107*, 14999–15004.
5. Mak, K. F.; Shan, J.; Heinz, T. F. Electronic Structure of Few-Layer Graphene: Experimental Demonstration of Strong Dependence on Stacking Sequence. *Phys. Rev. Lett.* **2010**, *104*, 176404.
6. Min, H.; MacDonald, A. H. Electronic Structure of Multilayer Graphene. *Prog. Theor. Phys. Suppl.* **2008**, *176*, 227–252.
7. Kumar, A.; Escoffier, W.; Poumirol, J. M.; Faugeras, C.; Arovas, D. P.; Fogler, M. M.; Guinea, F.; Roche, S.; Goiran, M.; Raquet, B. Integer Quantum Hall Effect in Trilayer Graphene. *Phys. Rev. Lett.* **2011**, *107*, 126806.
8. Otani, M.; Koshino, M.; Takagi, Y.; Okada, S. Intrinsic Magnetic Moment on (0001) Surfaces of Rhombohedral Graphite. *Phys. Rev. B* **2010**, *81*, 161403(R).
9. McCann, E.; Koshino, M. Spin-Orbit Coupling and Broken Spin Degeneracy in Multilayer Graphene. *Phys. Rev. B* **2010**, *81*, 241409(R).
10. Koshino, M.; McCann, E. Gate-Induced Interlayer Asymmetry in ABA-Stacked Trilayer Graphene. *Phys. Rev. B* **2009**, *79*, 125443.
11. Liu, Y.; Lew, W. S.; Goolaup, S.; Liew, H. F.; Wong, S. K.; Zhou, T. Observation of Oscillatory Resistance Behavior in Coupled Bernal and Rhombohedral Stacking Graphene. *ACS Nano* **2011**, *5*, 5490–5498.
12. Zou, K.; Zhang, F.; Clapp, C.; MacDonald, A. H.; Zhu, J. Transport Studies of Dual-Gated ABC and ABA Trilayer Graphene: Band Gap Opening and Band Structure Tuning in Very Large Perpendicular Electric Fields. *Nano Lett.* **2013**, *13*, 369–373.
13. Zhang, W.; Yan, J.; Chen, C.-H.; Lei, L.; Kuo, J.-L.; Shen, Z.; Li, L.-J. Molecular Adsorption Induces the Transformation of Rhombohedral- to Bernal-Stacking Order in Trilayer Graphene. *Nat. Commun.* **2013**, *4*, 2074.
14. Yankowitz, M.; Wang, J. I.-J.; Birdwell, A. G.; Chen, Y.-A.; Watanabe, K.; Taniguchi, T.; Jacquod, P.; San-Jose, P.; Jarillo-Herrero, P.; LeRoy, B. J. Electric Field Control of Soliton Motion and Stacking in Trilayer Graphene. *Nat. Mater.* **2014**, *13*, 786–789.
15. Tsen, A. W.; Brown, L.; Havener, R. W.; Park, J. Polycrystallinity and Stacking in CVD Graphene. *Acc. Chem. Res.* **2013**, *46*, 2286–2296.
16. Brown, L.; Hovden, R.; Huang, P.; Wojcik, M.; Muller, D. A.; Park, J. Twinning and Twisting of Tri- and Bilayer Graphene. *Nano Lett.* **2012**, *12*, 1609–1615.
17. Robertson, A. W.; Bachmatiuk, A.; Wu, Y. A.; Schäffel, F.; Rellinghaus, B.; Büchner, B.; Rümmeli, M. H.; Warner, J. H.

Atomic Structure of Interconnected Few-Layer Graphene Domains. *ACS Nano* **2011**, *5*, 6610–6618.

18. Warner, J. H.; Mukai, M.; Kirkland, A. I. Atomic Structure of ABC Rhombohedral Stacked Trilayer Graphene. *ACS Nano* **2012**, *6*, 5680–5686.

19. Cong, C.; Yu, T.; Sato, K.; Shang, J.; Saito, R.; Dresselhaus, G. F.; Dresselhaus, M. S. Raman Study on the G Mode of Graphene for Determination of Edge Orientation. *ACS Nano* **2011**, *5*, 8760–8768.

20. Lui, C. H.; Li, Z.; Chen, Z.; Klimov, P. V.; Brus, L. E.; Heinz, T. F. Imaging Stacking Order in Few-Layer Graphene. *Nano Lett.* **2011**, *11*, 164–169.

21. Chen, J. N.; Badioli, M.; Alonso-Gonzalez, P.; Thongrattanasiri, S.; Huth, F.; Osmond, J.; Spasenovic, M.; Centeno, A.; Pesquera, A.; Godignon, P.; et al. Optical Nano-Imaging of Gate-Tunable Graphene Plasmons. *Nature* **2012**, *487*, 77–81.

22. Fei, Z.; Rodin, A. S.; Andreev, G. O.; Bao, W.; McLeod, A. S.; Wagner, M.; Zhang, L. M.; Zhao, Z.; Thiemens, M.; Dominguez, G.; et al. Gate-Tuning of Graphene Plasmons Revealed by Infrared Nano-Imaging. *Nature* **2012**, *487*, 82–85.

23. Fei, Z.; Andreev, G. O.; Bao, W. Z.; Zhang, L. F. M.; McLeod, A. S.; Wang, C.; Stewart, M. K.; Zhao, Z.; Dominguez, G.; Thiemens, M.; et al. Infrared Nanoscopy of Dirac Plasmons at the Graphene-SiO$_2$ Interface. *Nano Lett.* **2011**, *11*, 4701–4705.

24. Huth, F.; Govyadinov, A.; Amarie, S.; Nuansing, W.; Keilmann, F.; Hillenbrand, R. Nano-FTIR Absorption Spectroscopy of Molecular Fingerprints at 20 nm Spatial Resolution. *Nano Lett.* **2012**, *12*, 3973–3978.

25. Kim, D. S.; Heo, J.; Ahn, S. H.; Han, S. W.; Yun, W. S.; Kim, Z. H. Real-Space Mapping of the Strongly Coupled Plasmons of Nanoparticle Dimers. *Nano Lett.* **2009**, *9*, 3619–3625.

26. Aizpurua, J.; Taubner, T.; de Abajo, F. J.; Brehm, M.; Hillenbrand, R. Substrate-Enhanced Infrared Near-Field Spectroscopy. *Opt. Express* **2008**, *16*, 1529–1545.

27. Wagner, M.; Fei, Z.; McLeod, A. S.; Rodin, A. S.; Bao, W.; Iwinski, E. G.; Zhao, Z.; Goldflam, M.; Liu, M.; Dominguez, G.; et al. Ultrafast and Nanoscale Plasmonic Phenomena in Exfoliated Graphene Revealed by Infrared Pump−Probe Nanoscopy. *Nano Lett.* **2014**, *14*, 894–900.

28. Chen, J. N.; Nesterov, M. L.; Nikitin, A. Y.; Thongrattanasiri, S.; Alonso-Gonzalez, P.; Slipchenko, T. M.; Speck, F.; Ostler, M.; Seyller, T.; Crassee, I.; et al. Strong Plasmon Reflection at Nanometer-Size Gaps in Monolayer Graphene on SiC. *Nano Lett.* **2013**, *13*, 6210–6215.

29. Berweger, S.; Nguyen, D. M.; Muller, E. A.; Bechtel, H. A.; Perkins, T. T.; Raschke, M. B. Nano-Chemical Infrared Imaging of Membrane Proteins in Lipid Bilayers. *J. Am. Chem. Soc.* **2013**, *135*, 18292–18295.

30. Bechtel, H. A.; Muller, E. A.; Olmon, R. L.; Martin, M. C.; Raschke, M. B. Ultrabroadband Infrared Nanospectroscopic Imaging. *Proc. Natl. Acad. Sci. U.S.A.* **2014**, *111*, 7191–7196.

31. Li, Z.; Lui, C. H.; Cappelluti, E.; Benfatto, L.; Mak, K. F.; Carr, G. L.; Shen, J.; Heinz, T. F. Structurally Dependent Fano Resonances in the Infrared Spectra of Phonons in Few-Layer Graphene. *Phys. Rev. Lett.* **2012**, *7*, 156801.

32. Ziegler, K. Scaling Behavior and Universality Near the Quantum Hall Transition. *Phys. Rev. B* **1997**, *55*, 10661.

33. Cvitkovic, A.; Ocelic, N.; Hillenbrand, R. Analytical Model for Quantitative Prediction of Material Contrasts in Scattering-Type Near-Field Optical Microscopy. *Opt. Express* **2007**, *15*, 8550–8565.

34. Hauer, B.; Engelhardt, A. P.; Taubner, T. Quasi-Analytical Model for Scattering Infrared Near-Field Microscopy on Layered Systems. *Opt. Express* **2012**, *20*, 13173–13188.

35. Gerber, J. A.; Berweger, S.; O'Callahan, B. T.; Raschke, M. B. Phase-Resolved Surface Plasmon Interferometry of Graphene. *Phys. Rev. Lett.* **2014**, *113*, 055502.

36. Novotny, L.; Hecht, B. *Principles of Nano-Optics*; Cambridge University Press: Cambridge, U.K., 2006.

37. Neaspec GmbH, Germany, www.neaspec.com.

38. McLeod, A. S.; Kelly, P.; Goldflam, M. D.; Gainsforth, Z.; Westphal, A. J.; Dominguez, G.; Thiemens, M. H.; Fogler, M. M.; Basov, D. N. Model for Quantitative Tip-Enhanced Spectroscopy and the Extraction of Nanoscale-Resolved Optical Constants. *Phys. Rev. B* **2014**, *90*, 085136.